Journal of Alloys and Compounds 735 (2018) 1119–1130

Contents lists available at ScienceDirect

Journal of Alloys and Compounds

journal homepage: http://www.elsevier.com/locate/jalcom

Spectral attributes of Eu^{3+} doped borotellurite glasses containing Mn_3O_4 nanoparticles

Siti Maisarah Aziz, M.R. Sahar*, S.K. Ghoshal

Advanced Optical Material Research Group, Department of Physics, Faculty Science, Universiti Teknologi Malaysia, 81310, Skudai, Johor Bahru, Johor, Malaysia

ARTICLE INFO

Article history:
Received 13 July 2017
Received in revised form
26 October 2017
Accepted 9 November 2017
Available online 14 November 2017

Keywords:
Borotellurite glass
Mn_3O_4 nanoparticles
Europium
Judd-Ofelt analysis
Magnetic properties

ABSTRACT

Glass samples of composition (59-*x*)TeO_2-30B_2O_3-10MgO-1Eu_2O_3-*x*Mn_3O_4, where $x = 0$, 0.5, 1.0, 1.5 and 2.0 mol % were prepared using melt quenching method. The Mn_3O_4 nanoparticles (MNPs) concentration dependent spectral properties were determined. XRD pattern verified the amorphous nature of prepared glasses and the presence of MNPs inside the glass matrix. TEM images revealed the nucleation of MNPs of average diameter 15 ± 1 nm. High resolution TEM data confirmed the NPs growth along (1 0 3) crystal plane orientation having lattice spacing ≈ 0.276 nm. Raman spectra displayed a shift in the vibrational modes of TeO_4 and TeO_3 units and thereby confirmed the alteration in the glass network structures mediated by NPs. The bonding characteristics of Eu^{3+} and ligand field parameters were evaluated. The observed increase in the network covalency was attributed to the MNPs assisted changes in the electron distribution. The emission spectra of glass samples revealed five prominent peaks centred at 578 nm, 591 nm, 610 nm, 651 nm and 700 nm which were assigned to the transition from $^5D_0 \rightarrow {}^7F_J$ (J = 0, 1, 2, 3, 4) states of Eu^{3+} ion. Judd-Ofelt intensity parameters were calculated. The prepared glasses exhibited paramagnetic behaviour. EPR spectra verified the predominant occurrence of Mn^{2+} with effective $g \approx 2.0$.

1. Introduction

Plasmonic nanoglass is a new research paradigm with numerous application possibilities. Metallic NPs (such as gold, silver, copper, etc.) embedded rare earth ions (REIs) doped glass became attractive during past two decades. The inclusion of gold (Au) and Ag (silver) NPs in glass containing REIs [1,2] were exploited to enhance the quantum efficiency to achieve high performance lasing glass system. Yusoff et al. [3] has proposed that the enhancement of photoluminescence intensity is deduced by energy transfer from NPs to REIs and large local field in the vicinity of the REIs. Previous research also demonstrated the impact of heat treatment on the overall properties of tellurite glass [4]. Appropriate assembling of nanoparticles generates new organized nanostructures with novel physical properties, which can be used for various applications in spintronics, ultrahigh density magnetic storage and magneto-optics device. Particularly, the development of spintronics requires new magnetic nanostructures with desired properties. Thus, efficient methods were demanded for preparing and assembling magnetic NPs based structures.

Lately, modification of electro-magneto-optic properties of REIs doped glass system by incorporating magnetic NPs generated renewed interests for magneto-optic device applications. As compared to their bulk counterpart, magnetic NPs possess several outstanding attributes including large specific surface area, low dimensionality and quantum confinement effect [5]. Furthermore, they exhibit high saturation field, high field irreversibility, and extra anisotropy contributions. Synthesis and characterization of magnetic (Fe, Co, Ni and Mn) NPs have ever-growing interest. Amongst all, Mn ions have been frequently used to improve the structural, electrical and magnetic properties of vitreous systems [6]. Manganese ions exist in different valence states in the glassy matrices. For example, Mn^{3+} ions in borate glasses exist with octahedral coordination whereas in silicate and germanate glasses they exist as Mn^{2+} ions with both octahedral and tetrahedral coordination [7]. Moreover, these well-known paramagnetic ions (Mn^{2+} and Mn^{3+}) are identified as strong luminescence activators [8]. On the top, incorporation of Mn_3O_4 in glass has paramount

* Corresponding author.
E-mail addresses: sitimaisarahaziz@yahoo.com (S.M. Aziz), mrahim057@gmail.com (M.R. Sahar).

https://doi.org/10.1016/j.jallcom.2017.11.123
0925-8388/

importance due to their excellent physical and structural properties [9]. These transition metal ions contribute multi-valence states in the glass network and remarkably influence the overall properties.

In the context of borotellurite (BT) glass, Yusub et al. [10] acknowledged the conversion of some BO_4 units into BO_3 units due to the increasing concentration of modifying manganese ions in the glass network. The alteration in the physical properties of BT glasses as a function of manganese concentration was attributed to the increase of non-bridging oxygen (NBO) in the BT network [11]. The incorporation of manganese in glass could open the network and create NBO. Consequently, the optical band gap (E_{opt}) was decreased and Urbach energy (ΔE) was increased [12]. However, the majority of these researches are related to the bulk manganese. Therefore, this present study aimed to investigate the impact of MNPs on the spectroscopic properties of BT glass.

It is worth noting that Judd-Ofelt (J-O) theory has not been applied so far to characterize the spectroscopic properties of Eu^{3+} ions doped BT glasses with NPs embedment. Peng and Izumitani [13] evaluated the J-O parameters for $^5D_0 \rightarrow {}^7F_2$, $^7F_4$ and $^7F_6$ emission transitions of the Eu^{3+} ions. Van Deun et al. [14] studied the absorption spectra of Eu^{3+} ions involving $^7F_0 \rightarrow {}^5D_2$,$^5D_4$ and $^5L_6$ transitions, where the calculated J-O parameters of Eu^{3+} ions [15] exhibited good agreement to the measured oscillator strengths. J-O parameters for glass containing magnetic NPs have not been reported in literature.

Efforts were seldom dedicated towards the incorporation of MNPs in BT glass system to examine their role in improving the structural, optical and magnetic properties. In this view, we prepared a new series of MNPs embedded BT glass doped with Eu^{3+} ions and characterized. The effects of MNPs concentration changes on the structural and luminescence properties were evaluated. The optical absorption spectra were used to estimate the bonding parameters of the prepared glasses. The local symmetry of the Eu^{3+} ions with their surrounding ligands was calculated. The J-O analysis was performed to calculate the oscillator strengths and intensity parameters (Ω_λ = 2, 4, 6). Then, the magnetic properties were accomplished from the magnetic moment of the local magnetic properties due to the nature of spin-spin interaction.

2. Materials and methods

Analytical grade powdered chemical reagents of high purity (Sigma Aldrich, 99.9%) such as Tellurium oxide (TeO_2), Boric acid (H_3BO_3), Magnesium oxides (MgO), Europium oxide (Eu_2O_3) and Manganese oxide (Mn_3O_4) were acquired for the glass preparation. The batch composition and the prepared sample designation are as follows:

BTMEMn0.0: 59TeO_2-30B_2O_3-10MgO-1Eu_2O_3-0.0Mn_3O_4

BTMEMn0.5: 58.5TeO_2-30B_2O_3-10MgO-1Eu_2O_3-0.5Mn_3O_4

BTMEMn1.0: 58TeO_2-30B_2O_3-10MgO-1Eu_2O_3-1.0Mn_3O_4

BTMEMn1.5: 57.5TeO_2-30B_2O_3-10MgO-1Eu_2O_3-1.5Mn_3O_4

BTMEMn2.0: 57TeO_2-30B_2O_3-10MgO-1Eu_2O_3-2.0Mn_3O_4

The required proportion of the glass constituents (nominal compositions) were weighed using high precession balance (Electronic Balance Precise XT 220A) and mixed thoroughly for about 30 min using milling machine to ensure homogeneous mixing. Melt-quenching method was used to prepare these glass samples. A platinum crucible containing about 20 g of the mixed glass constituents was placed in a furnace at 900 °C for 1 h. For homogeneous mixing, the molten liquid is shaken frequently and vigorously. Then, the melt was poured in a brass mould once the desired viscosity was achieved. Subsequently, the sample was transferred to an annealing furnace at 300 °C and kept inside for 3 h to remove the thermal and mechanical strains completely. Afterward, the furnace was switched off and the samples were cooled down to room temperature. The obtained glass samples were cut and polished for further characterizations.

The amorphous phases of the synthesized samples were identified using X-ray Diffraction (XRD) measurement (Siemens Diffractometer D5000) in the 2θ range of 10°–90°. The bonding vibrational modes in the range of 200–1600 cm^{-1} are captured using Raman Spectroscopy (Horiba Jobin Yvon, HR800 UV). The formation crystalline lattice plane in MNPs was confirmed using HRTEM (JEOL 2100F) operated at an acceleration voltage of 200 kV where a small amount of powder sample was dispersed into acetone liquid using ultrasonic bath. The solution was then placed onto a copper grid and allowed to dry before it was ready for characterization. Absorption spectra in the range of 200–800 nm were recorded using Shimadzu 3101 PC UV-VIS-NIR scanning spectrometer.

The Nephelauxetic ratio (β) was calculated via [16],

$$\beta = \frac{\bar{v}_c}{\bar{v}_a} \tag{1}$$

where $\bar{v}_c$ is the wavenumber (in cm^{-1}) of a particular transition of the RE ion and $\bar{v}_a$ is the corresponding wavenumber (in cm^{-1}) for the transition of an aquo-ion [17]. Both $\bar{v}_c$ and $\bar{v}_a$ are obtained from UV–Vis optical absorption spectra. The bonding parameter (δ) was determined using [16],

$$\delta = \frac{1 - \bar{\beta}}{\bar{\beta}} \tag{2}$$

where $\bar{\beta}$ is the average value of β. Positive sign of δ represents the covalent bonding and negative one signifies the ionic bonding. The luminescence spectra and decay time of the samples with various concentrations of MNPs were recorded by a JASCO FP-8500 Series with a 150 W xenon lamp as excitation source. The spectra were measured in the wavelength range of 200–800 nm. Finally, to determine concentration dependent MNPs embedded BT glass on magnetic properties via Vibrating Sample Magnetometer (VSM) and Electron Spin Resonance (ESR). All the measurement was carried out at room temperature. The colour of glass sample without MNPs was pale yellow. With the increase of MNPs concentration in the glass the sample colour was changed from yellow to brownish purple. This colour change indicated the successful embedment of MNPs into the glass matrix and subsequent alteration in the overall properties. Table 1 enlists the calculated physical and optical properties of studied glasses.

3. Results and discussion

3.1. XRD pattern and Raman spectra

Fig. 1 shows the typical XRD pattern of BTMEMn2.0 glass. The occurrence of strong diffraction peak at $2\theta = 16°$, 28°, 31°, and 37° were allocated to the crystalline MNPs having (101), (112), (103), and (211) planes, respectively. All the XRD peaks were perfectly indexed to the MNPs single phase (JCPDS Card 24–0734) [18]. In addition, the average crystallite size was estimated to be 6.48 ± 0.48 nm. Debye Scherrer formula was used for the most intense peak (112) peak to estimate the nanocrystallite sizes.

The occurrence of prominent bands in the Raman spectra (Fig. 2) clearly revealed the presence of various structural units in the glass

Table 1
Physical and optical properties of all BT glass samples.

Properties	BTMEMn0.0	BTMEMn0.5	BTMEMn1.0	BTMEMn1.5	BTMEMn2.0
ρ (g/cm^3)	4.717	4.716	4.706	4.725	4.736
V_m	25.90	25.92	25.98	25.71	25.58
n	2.32	2.38	2.50	2.43	2.41
V_t	0.26	0.21	0.16	0.17	0.18
Λ	0.800	0.799	0.798	0.797	0.796
OPD (g atml^{-1})	85.04	85.16	85.12	85.62	85.96
α_e (10^{-22} cm^{-2})	6.12	6.27	6.55	6.33	6.27
R_m (cm^3 mol^{-1})	15.44	15.81	16.52	15.97	15.81
λ_o (nm)	4.40	4.42	4.44	4.37	4.35
E_g (eV)	3.27	3.03	2.61	2.87	2.91
ΔE (eV)	0.28	0.41	0.68	0.52	0.49

system. The broad band near 450-485 cm^{-1} indicated the characteristic of the bending and stretching vibrations modes of the Te-O-Te or O-Te-O linkages wherein the oxygen was in the position of axial and equatorial to the tellurium atom [19]. The appearance of the broad band around 665-682 cm^{-1} and at 750-778 cm^{-1} confirmed the presence of stretching vibration mode between tellurium atom and bridging oxygen in the TeO_4 tbp units and vibration of the TeO_3 tp units with non-bridging oxygen (NBO), respectively. Table 1 enlists the physical and optical properties of the prepared glass system. Table 2 compares the observed Raman bands with other BT glass system. The band corresponding to TeO_4 tbp group exhibited a slight shift towards higher wavenumber which indicated the structural alteration. Furthermore, as the amount of MNPs was increased to 1.0 mol %, the peak of TeO_4 tbp was displaced from 665 cm^{-1} to 682 cm^{-1}. Beyond 1.0 mol % of MNPs, the peak was shifted towards a lower wavenumber (678 cm^{-1} and 667 cm^{-1}). Meanwhile, the TeO_3 tp group was shifted towards a higher wavenumber as MNPs is added up to 1.0 mol% and decreased afterward. The dominance of Te -O vibration compare to borate groups was attributed to the easy polarization of TeO_2 units than B_2O_3 units. Thus, the Raman peak intensities of B_2O_3 were relatively weaker than that of TeO_2. These results authenticated the building up of the glass structure with combination of both tellurite and borate networks.

The good correspondence between the phonon energies involved in the electronic transitions and the vibrational modes

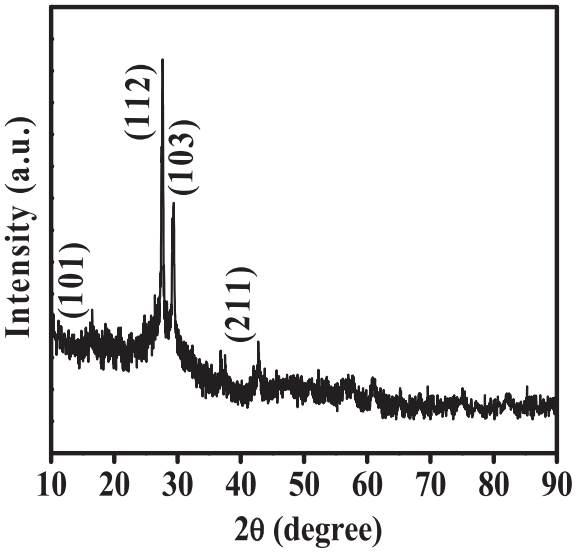

Fig. 1. Typical XRD pattern of BTMEMn2.0 glass.

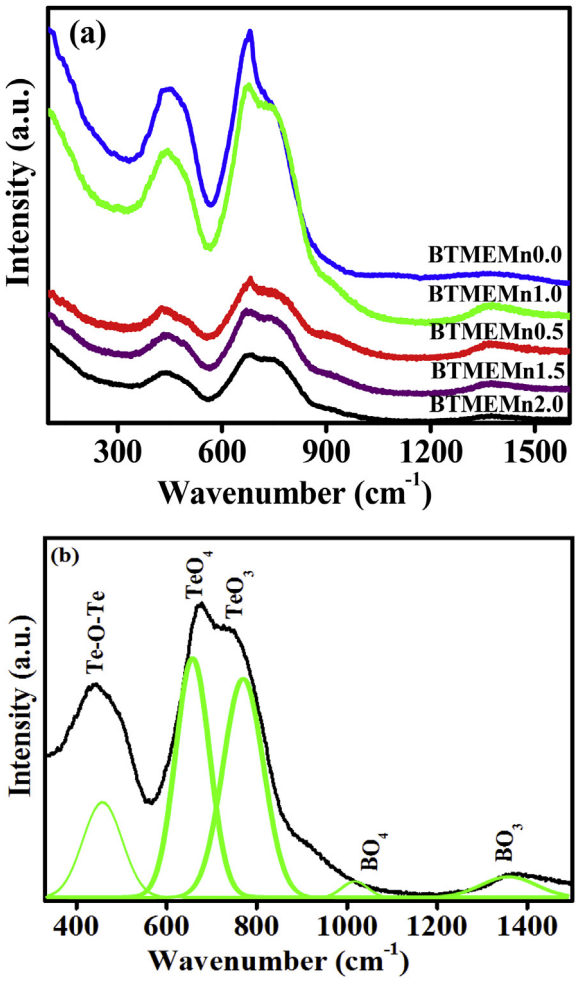

Fig. 2. (a) Raman spectra of all synthesized BT glass system, and (b) the de-convoluted spectra of BTMEMn1.0 sample.

observed in the Raman spectra demonstrated the local perturbation effects due to the accommodation of small amounts of MNPs. The MNPs concentration dependent Raman shift in the symmetrical vibrational modes of TeO_2 and TeO_4 groups towards higher wavenumber further verified the influence of NPs on glasses structures. It was affirmed that the covalency and asymmetry between Eu–O bond and ligands can be enhanced by increasing the MNPs content. The vibrational modes involved in the progressions corresponded to lattice phonons. This result was interpreted in terms of the ion–lattice interaction mechanisms, which aroused due to the occupation of MNPs along the interconnected Te-O-Te network in the vicinity of Eu^{3+} ion. This in turn altered the symmetry and/or covalency of the glass at the Eu^{3+} ion site. The nature of the Raman spectra suggested the presence of an increasing degree of disorder with increasing content of MNPs. This was due to the strong dependence of absorption frequencies on the nature of anions rather than cations. The concentration of the bonding defects was found to depend upon the concentration of MNPs. Thus, MNPs concentration variation caused substantial structural modifications at the Eu^{3+} ions site in BT glass network.

The local field emanating from MNPs has affected different structural units of tellurite, borate and linkages between them. The Eu^{3+} ions that occupy different coordination sites with non-centrosymmetric potential contributed significantly to Ω_2. The variations in the non-centro-symmetric potential sites generated a change in the dielectric properties of the media. Consequently, the

Table 2
Comparison of assigned Raman bands of the present glasses with other reported BT glass systems.

Glass system	Te-O-Te	Band Assignments (cm^{-1})				Ref.
		TeO_4 (tbp)	TeO_3 (tp)	BO_4 unit	BO_3 unit	
B_2O_3-TeO_2-Bi_2O_3-ZnO	455	670	750	–	1350	[20]
TeO_2-B_2O_3-Al_2O_3	450	665	762	–	–	[21]
Na_2O-B_2O_3-TeO_2	453	679	778	–	–	[22]
TeO_2-B_2O_3-ZnO-V_2O_5	464	671	750	935	–	[23]
BTMEMn0.0	450	665	760	1053	1373	Present work
BTMEMn0.5	459	674	762	1135	1367	Present work
BTMEMn1.0	471	682	775	1177	1363	Present work
BTMEMn1.5	468	678	768	1147	1363	Present work
BTMEMn2.0	466	667	763	1072	1365	Present work

environment of the Eu^{3+} ions and nephelauxetic ratio influenced the Ω_2 value. In fact, among the three J-O parameters, the parameter Ω_2 was related to the covalency and structural changes in the vicinity of the REI (short-range effect). Conversely, Ω_4 and Ω_6 being related to the long-range effects were strongly influenced by the vibrational levels associated with the central REI bound to the ligand atoms. This change proved that the polarizability of the glass matrix was enhanced with increasing MNPs concentration.

3.2. TEM analysis

Fig. 3 (a) shows the magnified (at 50 nm) HR-TEM image of BTMEMn2.0 glass sample. Homogeneously dispersed tiny spherical and non-spherical black blobs in the micrograph manifested the existence of MNPs in the glass matrix. Moreover, the occurrence of bigger NPs with different size and shapes were attributed to the Ostwald's ripening growth mechanism assisted coalescence of smaller NPs. Additionally, these NPs revealed agglomeration tendency [24]. The region marked by the yellow rectangle in Fig. 3(a) was enlarged and shown in Fig. 3(b). It displayed the single particle in BTMEMn2.0 glass sample for two different magnifications (20 nm and 5 nm). Fig. 3 (c) illustrates the further enlargement of yellow box in (b) indicating the d-spacing (d = 0.276 nm). The selected area electron diffraction (SAED) pattern as depicted in Fig. 3 (d) provided the information of lattice parameter which is well matched with XRD pattern. The SAED pattern in the presence of ring and spot indicated the polycrystalline nature of MNPs. These spots presented the reflections of both compounds which were well resolved in the XRD pattern. These rings were assigned to the nucleation of small crystallites while the spots were allocated to formation of the large nanocrystallites in the glass matrix [25]. The strong diffraction ring corresponds to the (103) plane of nanocrystallited which was comparable to MNPs lattice spacing of 0.276 nm (JCPDS No. 24–0734) [18]. Fig. 3(e) depicts that the NPs size distribution is Gaussian with average diameter about 15 ± 1 nm.

3.3. Absorption spectra

Fig. 4 shows a typical optical absorption spectrum of BTMEMn0.0 glass sample in the wavelength range of 400–650 nm which exhibited three prominent bands at around 461 nm, 531 nm and 591 nm corresponding to $^7F_0 \rightarrow {}^5D_2$, $^7F_0 \rightarrow {}^5D_1$ and $^7F_0 \rightarrow {}^5D_0$ transitions.

Using the absorption data the bonding properties of Eu^{3+}–O and surrounding ligand field parameters inside the glass matrix were calculated. The bonding parameter (δ) was calculated from the obtained nephelauxetic ratio. The values of β and δ are listed in Table 3. It was observed that the δ possessed a positive sign (Table 3), implying covalent bonding nature of Eu^{3+}-ligand with increasing concentration of MNPs. This increment in δ was ascribed to the value of electronegativity difference. With increasing electronegativity difference between two atoms, the polar covalent bond became higher. This signified that one of the atoms was more positive and the other one was more negatively charged. The atom which attracted electrons toward it became more negative and vice versa. The electronegativity of Mn was 1.55, oxygen was 3.61 and Te was 2.15 which showed that the electronegativity difference between Mn-O was higher than those of Te-O bond. Thus, the addition of MNPs at the expense of TeO_2 caused an increase in the number of covalence bond. The electron pair in Mn-O bonding was shifted towards the oxygen atom because of the larger electronegativity value of oxygen.

The alteration in covalency and the ligand environment around the Eu^{3+} ion site was affected by the increase in NBO which in turn modified the covalency of the metal-ligand bond in the glasses. However, beyond 1.0 mol % of MNPs the observed reduction in the value of δ indicated an increase in the ionic type of bonding. The relation of δ was inversely proportional to that of β as found in other glass systems. The decrement in the β was caused by the decreasing of effective positive charge connected to europium atom when it attracted electrons from ligands. The gradual expansion of the d-orbital of Eu^{3+} ions produced a larger electron cloud and simultaneously allowed the overlap of ligand orbital and d-orbital of europium. This led to a decrease in the inter-electronic repulsion between europium and ligand, thereby increased the covalence bonds. The size of orbital became larger than the single orbital resulted from the overlapping of two atomic orbitals.

Effectively, the bonding characteristic between Eu^{3+} ion and ligands in the glass matrix and the asymmetrical site around Eu^{3+} ions were considerably changed due to the embedment of MNPs. Moreover, the lower the value of nephelauxetic ratio signified the larger electron cloud generated in the glass sample. It enhanced the tendency of atomic orbitals overlapping between Eu^{3+} ion orbital and ligand orbitals. Thus, the value of bonding parameter was increased, implying an enhanced covalency.

3.4. Luminescence spectra

Fig. 5 displays the room temperature luminescence spectra of all BT glass samples under the excitation wavelength (λ_{exc}) of 390 nm. It is comprised of five significant bands centred around 578 nm, 591 nm, 614 nm, 651 nm and 700 nm which were assigned to the transitions of $^5D_0 \rightarrow {}^7F_0$, $^5D_0 \rightarrow {}^7F_1$, $^5D_0 \rightarrow {}^7F_2$, $^5D_0 \rightarrow {}^7F_3$, and $^5D_0 \rightarrow {}^7F_4$, respectively. Emission bands located in the region of 580–620 nm were more affected by the dopant concentration due to spin reversal, where some of the singlet states have been converted to the triplet one [26]. Mn^{2+} being paramagnetic in nature could influence the ligand Eu^{3+} ions interactions. Due to high energy phonons in the glasses, the emissions from the excited levels ^5D_J

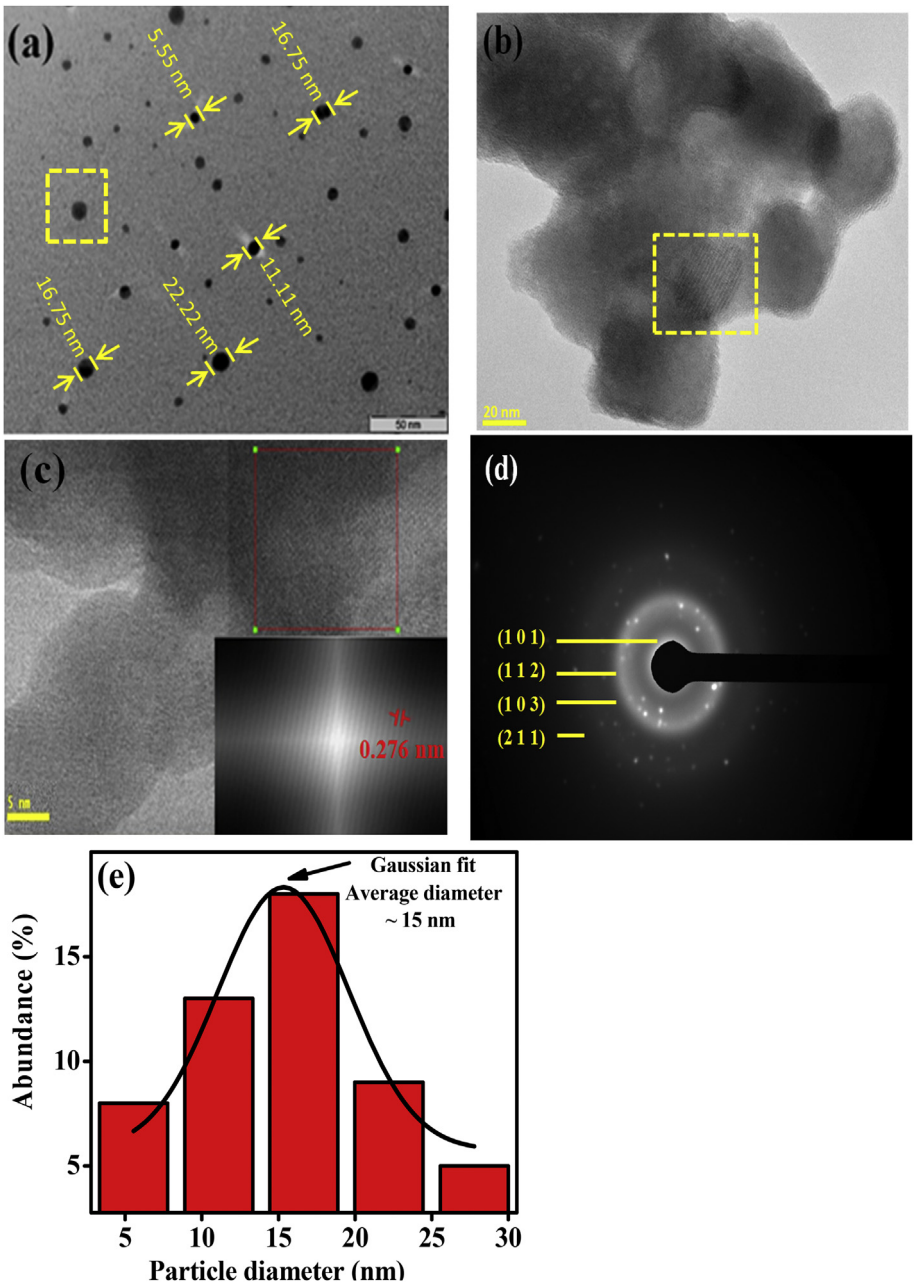

Fig. 3. HR-TEM images of the BTMEMn2.0 glass at the magnification of (a) 50 nm, (b) 20 nm, (c) lattice spacing of (103) lattice plane direction, (d) SAED pattern of the red box in (c), and (e) NPs size distribution corresponding to 50 nm magnification. (For interpretation of the references to colour in this figure legend, the reader is referred to the web version of this article.)

(J = 1,2) undergo a fast non-radiative transition at $^5D_0$ level when the Eu^{3+} ions were excited to any level above the $^5D_0$ level. The intensity of emission bands were diminished due to the increase of MNPs concentration, which was attributed to quenching effect [26].

It was evident (Fig. 5) that the intensity for $^5D_0 \rightarrow {}^7F_2$ (614 nm) transition is maximum compared to the others while it was minimum for $^5D_0 \rightarrow {}^7F_3$ (651 nm) transition. The $^5D_0 \rightarrow {}^7F_J$ (J = 5,6) transitions were not evidenced due to detectors limitations in the spectrofluorimeter. The intensity for $^5D_0 \rightarrow {}^7F_2$ dipole (ED) ($\Delta J = 2$) transition was about three times higher than the one with magnetic dipole (MD) transition ($\Delta J = 1$) $^5D_0 \rightarrow {}^7F_1$. These two transitions constituted the spin forbidden emission bands with ($\Delta S = 1$) [27]. The $^5D_0 \rightarrow {}^7F_{1,3}$ transitions were magnetic-dipole allowed which obeyed the selection rule of $|\Delta S| = 0$, $|\Delta L| = |\Delta J| \leq 1$ except ($0 \leftrightarrow 0$, $\Delta 1 = 0$) and less sensitive to the symmetry of the ligand environment around the Eu^{3+} ion site [27,28]. Besides, the $^5D_0 \rightarrow {}^7F_{2,4}$ transitions were electric-dipole allowed and obeyed the selection rule of $|\Delta S| = 0$, $|\Delta L| = |\Delta J| \leq 6$, unless J or $J' = 0$ when $|\Delta J| = 2, 4, 6$, $\Delta I \pm 1$ [29]. It strongly depended on the local symmetry around the Eu^{3+} ions where the intensities were sensitive on the change in polarizability of the ligand atoms. In the present study, interactions of electromagnetic radiation due to the surface plasmon resonance of MNPs also contributed to the intensity changes in the ED and MD transitions. Asymmetric ratio (I_{AS}) was defined as the ratio of integral intensity of the ED transition ($^5D_0 \rightarrow {}^7F_2$) to the MD transition ($^5D_0 \rightarrow {}^7F_1$). The expression for I_{AS} yields [30],

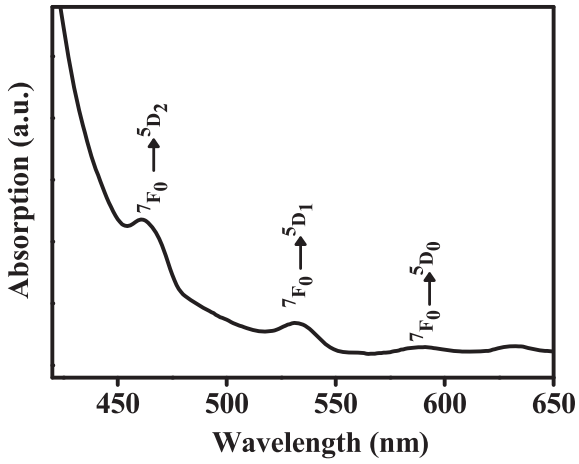

Fig. 4. Absorption spectrum of BTMEMn0.0 glass.

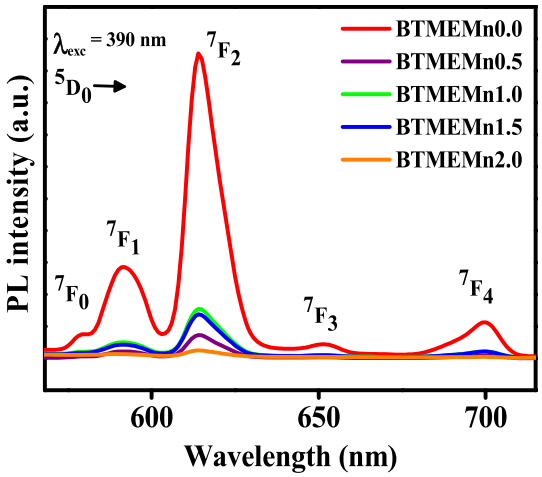

Fig. 5. Luminescence spectra of Eu^{3+} doped and MNPs embedded BT glasses.

$$I_{AS} = \frac{\int I_{0\rightarrow 2}(w)dw}{\int I_{0\rightarrow 1}(w)dw} \quad (3)$$

Values of I_{AS} provide important information about the symmetry of the ligand field and covalency of the metal-ligand bond. The I_{AS} values for BTMEMn0.0, BTMEMn0.5, BTMEMn1.0, BTMEMn1.5, BTMEMn2.0 glasses were found to be 4.09, 4.18, 4.87, 4.80 and 4.48, respectively. The higher I_{AS} values indicated that the Eu^{3+} ions were located in a higher asymmetrical environment due to the aggregation of MNPs. The calculated value of I_{AS} was slightly increased with the increase of MNPs concentration up to 1.0 mol % and decreased thereafter. The decrease in I_{AS} values might be due the transformation of singlet to triplet state in the presence of the spin orbital coupling effect [26]. The ratio of ED transition ($^5D_0$-$^7F_0$) to MD transition ($^5D_0$-$^7F_1$) is insignificant since the emission peak of $^7F_0$ was very weak. Meanwhile, laser integrated ratio (LIR) of the corresponding transition from ED ($^5D_0 \rightarrow {}^7F_2$) to the MD ($^5D_0 \rightarrow {}^7F_1$) was calculated, which was used to determine the degree of asymmetry in the vicinity of Eu^{3+} ions and Eu–O covalence [31]. The calculated values of LIR were ranged from 4.19 to 4.72, revealing that Eu^{3+} ions occupied a site without inversion symmetry.

Amongst all glasses, BTMEMn1.0 sample possessed higher magnitude of LIR and followed the trend of BTMEMn1.0 (4.72) > BTMEMn1.5 (4.70) > BTMEMn2.0 (4.33) > BTMEMn0.5 (4.22) > BTMEMn0.0 (4.19). These values were higher than those reported for the glass system such as Tellurite (2.78) [32], Borophosphate (2.15) [33] Silicate (3.19) [34] and Phosphate (3.64) [35]. The higher LIR values implied stronger covalent nature of bonding which was further supported by the bonding parameter data. These values were above 1.0 for centro-symmetric and were below 1.0 for non-centro-symmetric surroundings.

Fig. 6 illustrates the partial energy level diagram of Eu^{3+} ion which appears in the proximity of MNPs. Various mechanism such as ground state absorption, energy transfer from NP to the REI, radiative and nonradiative decay are shown. Upon laser excitation, the electrons undergo a transition from the ground state ($^7F_0$) to higher excited state $^5L_6$ via ground state absorption (GSA) process. Simultaneously, MNPs transfer an extra energy to Eu^{3+} ions. Thereafter, fast non-radiative (NR: $^5L_6 \rightarrow {}^5D_{2,1,0}$) and radiative (R: $^5D_0 \rightarrow {}^7F_{0,1,2,3,4}$) decay processes through multiphoton relaxation tend to populate the states. The $^5D_0$ to $^7F_{0,1}$ transitions responsible for the orange emission and the rest lie on red emissions at 610 nm, 651 nm and 700 nm. Conversely, the observed PL intensity quenching is due to the energy transfer from Eu^{3+} to Mn species. This energy transfer arises due to the nucleation and aggregation of large number of NPs in the immediate neighbourhood of Eu^{3+} ions. Such clustering of several tiny MNPs cause an overlapping of the electric field and thus reduce the local field effect mediated energy transfer from MNPs to Eu^{3+} ion. Meanwhile, this transfer could be due to singlet to triplet states transformation [26].

3.5. Judd–Ofelt analysis

Almost over half century, the Judd-Ofelt (J-O) [15,36] theory was broadly used to evaluate the spectroscopic quality of REIs doped materials. It was routinely used to calculate the oscillator strength for an induced electric dipole transition from ground state $^7F_0$ to an excited state. The value of oscillator strengths, (f) was calculated using the expression [36],

$$f = \frac{8\pi^2 mc\nu}{3h(2J+1)} \frac{(n^2+2)^2}{9n} \sum_{\lambda=2,4,6} \Omega_\lambda \left(\Psi J \left\| U^\lambda \right\| \Psi' J'\right)^2 \quad (4)$$

where n is refractive index of the medium, J is the total angular momentum of the ground state degenerated $2J + 1$ Stark level, ν is the wavenumber of the transition, Ω_λ ($\lambda = 2, 4, 6$) are J-O intensity parameters and $\|U^\lambda\|^2$ ($\lambda = 2, 4, 6$) are the doubly reduced matrix

Table 3
Band positions (cm^{-1}) and bonding parameter (β and δ) of the prepared glass system.

Transition	BTMEMn0.0	BTMEMn0.5	BTMEMn1.0	BTMEMn1.5	BTMEMn2.0	Aquo-ion [17]
$^7F_0 \rightarrow {}^5D_2$	21459	21321	21231	21459	21505	21519
$^7F_0 \rightarrow {}^5D_1$	18656	18761	18796	18939	18903	18691
$^7F_0 \rightarrow {}^5D_0$	17035	17035	17035	17094	17152	17277
β	0.9941	0.9935	0.9926	1.0000	1.0012	–
δ	0.5896 ± 0.035	0.6477 ± 0.038	0.7448 ± 0.044	−0.0086 ± 0.0005	−0.1268±-0.076	–

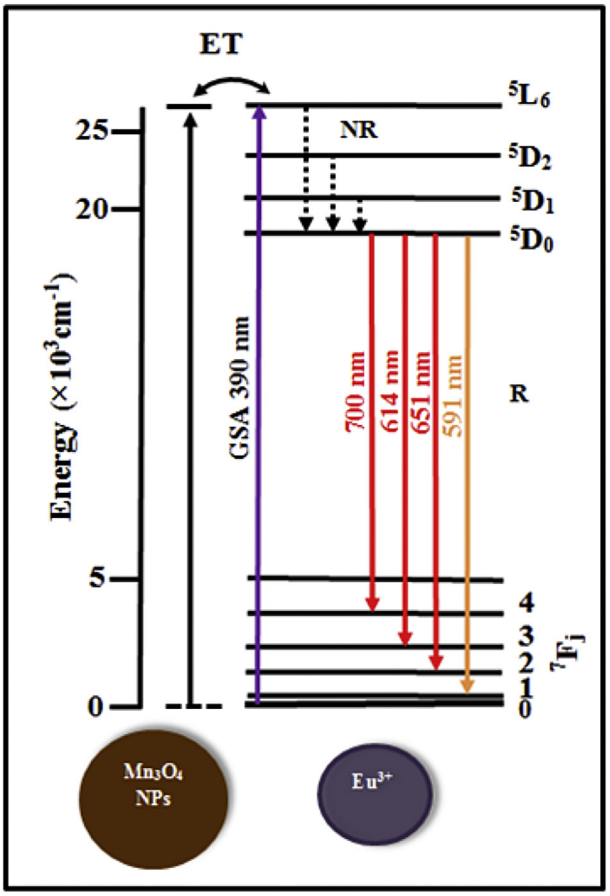

Fig. 6. Partial energy diagram of Eu^{3+} ion in the vicinity of MNPs inside the BT glass matrix (ET: Energy Transfer, R: Radiative Decay and NR: Nonradiative Decay).

elements evaluated using intermediate coupling approximation for $\Psi J \rightarrow \Psi' J'$ a transition.

The transition intensity depends on the $\|U^{\lambda}\|^2$ values between ΨJ and $\Psi' J'$ manifold. J-O analysis for Eu^{3+} ion was challenging due to the unavailability of some transitions in the optical absorption spectra including $^7F_0$ and $^7F_1$ to $^5D_1$,$^5D_2$ and $^5L_6$ states. In addition, the ground state ($^7F_0$) and first excited state ($^7F_1$) in the Eu^{3+} ion were being close to each other (energy gap ~350 cm^{-1}) resulted the availability of 30% population in the $^7F_1$ state [29]. Consequently, the J-O model was responsible for thermal correction to the oscillator strength of the corresponding transitions of Eu^{3+} doped glass matrices. The observed bands of Eu^{3+} in the UV–Vis absorption spectra were not sufficient to fit using this procedure since Eu^{3+} ion possessed low-lying allowed charge transfer band. This in turn led to a breakdown of the J-O theory. Partly, Eu^{3+} ion was not well suited for J-O analysis, in contrast to other trivalent lanthanide (Ln^{3+}) ions. These limitations were overcome by calculating the J-O intensity parameters using the emission data instead of the absorption spectra. Nevertheless, the J-O parameters of Eu^{3+} ions calculated from absorption and emission spectra agreed well when the thermal correction was applied to the oscillator strengths of the transitions.

In the present work luminescence spectra were used as an alternative approach following [13] to find the J-O parameters of the prepared Eu^{3+} doped BT glasses containing MNPs. Due to selection rules and the unique nature of transition intensities for Eu^{3+} ion, any one of the $\|U^{\lambda}\|^2$ parameters decided the intensities of the transitions since the remaining two were zero [37]. Most of the matrix elements for transitions starting from the $^5D_0$ level were zero, except those for the $^5D_0 \rightarrow {}^7F_2$ transition (U(2) = 0.0032), $^5D_0 \rightarrow {}^7F_4$ transition (U(4) = 0.023) and $^5D_0 \rightarrow {}^7F_6$ transition (U(6) = 0.0002) as enlisted in Table 4.

The three phenomenological intensity parameters Ω_λ (λ = 2, 4, and 6) described the intensity of induced electric dipole transitions. According to J-O theory, it can be determined by a standard least-squares fitting approach of Eq. (4). All of the emission transitions of Eu^{3+} ions, and the magnetic dipole allowed transition $^5D_0 \rightarrow {}^7F_1$ were independent of the host matrix. Whereas, the induced electric dipole transitions $^5D_0 \rightarrow {}^7F_J$ (J = 2, 4, 6) were strongly depended on the host matrix. Thus, Ω_λ (λ = 2, 4, 6) parameters was evaluated solely from the emission transitions of $^5D_0 \rightarrow {}^7F_2$, $^5D_0 \rightarrow {}^7F_4$ and $^5D_0 \rightarrow {}^7F_6$, respectively. The Ω_λ parameters were simply be evaluated from the intensity ratio of the $^5D_0 \rightarrow {}^7F_J$ (J = 2 and 4) transitions ($\int I_J d\nu$) to the intensity of the $^5D_0 \rightarrow {}^7F_1$ transition ($\int I_1 d\nu$) using the relation [38],

$$\left|\frac{\int I_J d\nu}{\int I_1 d\nu}\right| = \frac{A_J}{A_1} = \frac{e^2}{S_{md}}\left(\frac{\nu_J}{\nu_1}\right)^3 \frac{n(n^2+2)^2}{9n^3}\Omega_\lambda\left(\Psi J\left\|U^{\lambda}\right\|\Psi' J'\right)^2 \quad (5)$$

where ν_1 and A_1 are the wavenumber and radiative transition probability of the magnetic dipole $^5D_0 \rightarrow {}^7F_1$ transition, $S_{md} = 7.83 \times 10^{-42}$ [39] which refers to the $^5D_0 \rightarrow {}^7F_1$ transition of Eu^{3+} ions MD transition, whose line strength is independent from the host composition or the ionic concentration. Similarly, ν_J and A_J are the wavenumber and radiative transition probability of the $^5D_0 \rightarrow {}^7F_J$ (J = 2 and 4) transitions and $\|U^{\lambda}\|^2$ are the doubly reduced square matrix elements (Table 4).

It is well known that the Ω_2 parameter is structure sensitive and depends on the covalence nature of the RE ion sites. The higher values of Ω_2 indicated the presence of covalent bonding between Eu^{3+} ions and their surrounding ligands as well as the asymmetric of the local environment of Eu^{3+} site [40,41]. Additionally, the higher ligand polarizability was responsible for higher overlap between the REIs and ligand orbitals. This imparted higher degree of covalency between the REIs and ligands. It is worth mentioning that the oxygen ion has higher electronegativity (3.44) compared to other anions. Consequently, the covalency of RE-O bonds was smaller than other RE-anion bonds. This led to the reduction of the Ω_2 values in BTMEMn glass. Meanwhile, the Ω_4 and Ω_6 corresponded to the viscosity and rigidity of the host medium in which the ions were situated [42].

Generally, Ω_6 parameter was not reported in the literature partly because of its negligible contribution to the lifetime of Eu^{3+} ions. The determined values Ω_2 and Ω_4 of Eu^{3+} ions for various concentrations of MNPs are listed in Table 5. Compared to Eu^{3+} doped other host matrices, BTMEMn glass system showed similar trends in the bonding parameter ($\Omega_2 > \Omega_4$). This explained the existing covalence character between the Eu^{3+} ion and ligands. Thus, BTMEMn glass revealed the relative asymmetry at the Eu^{3+} site and

Table 4
Wavenumbers and reduced matrix elements for $^5D_0 \rightarrow {}^7F_{J'}$ (J' = 0–6) transitions in the studied glass system.

Transition $^5D_0 \rightarrow$	Type	ν (cm^{-1})	$\|U^2\|^2$	$\|U^4\|^2$	$\|U^6\|^2$
$^7F_0$	Forbidden	17301.03	0	0	0
$^7F_1$	Magnetic dipole	16920.47	0	0	0
$^7F_2$	Electric dipole	16286.64	0.0032	0	0
$^7F_3$	Forbidden	15360.98	0	0	0
$^7F_4$	Electric dipole	14306.15	0	0.0023	0
$^7F_5$	Forbidden	–	0	0	0
$^7F_6$	Electric dipole	–	0	0	0.0003

covalent Eu–O bond character. These results were supported by the luminescence intensity ratio values. The calculated dipole line strengths were used to evaluate electric (A_{ed}) and magnetic (A_{md}) dipole radiative transition probabilities according the following expressions [41],

$$A_{ed} = \frac{64\pi^4 e^2 \nu^3}{3h(2J+1)} = \frac{n(n^2+2)^2}{9}\sum_{\lambda} =_{2,4,6}\Omega_\lambda \left(\Psi J \left\| U^\lambda \right\| \Psi' J'\right)^2 \quad (6)$$

$$A_{md} = \frac{64\pi^4 \nu^3 n^3}{3h(2J+1)}[S_{md}] \quad (7)$$

where e, λ, h and n have their usual meaning. The refractive index for the BTMEMn1.0 glass was found to be 2.5, which was comparable to values reported for similar compositions [37,42].

The radiative transition probability (A) for a transition $\Psi J \rightarrow \Psi' J'$ was obtained by summing up the A_{ed} and A_{md} [41],

$$A_T(\Psi J, \Psi' J') = A_{ed} + A_{md} \quad (8)$$

The total radiative transition probability (A_T) for an excited state is given as the sum of the $A(\Psi J, \Psi' J')$ terms calculated over all the terminal states. The relaxation of the excited state ΨJ to several lower-lying states $\Psi' J'$ was expressed by the radiative branching ratio β_R defined as [41],

$$\beta_R(\Psi J, \Psi' J') = A(\Psi J, \Psi' J')/A_T(\Psi J) \quad (9)$$

This rate of depopulation of an excited state was given by the radiative lifetime, $\tau_R(\Psi J)$,

$$\tau_R(\Psi J) = 1/A_T(\Psi J) \quad (10)$$

Stronger emission probabilities and more transitions from a level lead to faster decay and shorter lifetimes. The peak stimulated emission cross-section σ (λ_p) between the states (ΨJ) and ($\Psi' J'$) having a probability of $A(\Psi J, \Psi' J')$ was expressed as [41],

$$\sigma(\lambda_p)(\Psi J, \Psi' J') = \frac{\lambda_p^4}{8\pi c n^2 \Delta\lambda_{eff}} A(\Psi J, \Psi' J') \quad (11)$$

where c is the speed of light, λ_p the peak wavelength, and $\Delta\lambda_{eff}$ is the effective bandwidth of the emission peak found by dividing the integrated area of the emission band by its average height.

The radiative parameters such as emission band position (λ_p, nm), effective bandwidth ($\Delta\lambda_{eff}$, nm), radiative transition probability (A,s^{-1}), stimulated emission cross-section ($\sigma \times 10^{-22}cm^2$), branching ratios ($\beta_R$), experimental ($\tau_{exp}$) and calculated ($\tau_{cal}$) lifetimes corresponding to the $^5D_0 \rightarrow {}^7F_0$, $^5D_0 \rightarrow {}^7F_1$, $^5D_0 \rightarrow {}^7F_2$, $^5D_0 \rightarrow {}^7F_3$ and $^5D_0 \rightarrow {}^7F_4$ emission transitions of the Eu^{3+} ions in the prepared glasses were calculated and presented in Table 6. All the results for the $^5D_0 \rightarrow {}^7F_2$ transition are higher. The stimulated emission cross-section and branching ratio were the important laser parameters in the design of new luminescent devices. The higher values of these parameters predict the higher luminescence efficiency of the glasses. Furthermore, the achieved values of β_R are 50% higher than BTMEMn glass system.

It was established that such compositions have great potential for laser fabrication. The stimulated emission cross-section is often used as a parameter to lasing potential. In the present case, the obtained stimulated emission cross-section and the branching ratio values corresponding to the $^5D_0 \rightarrow {}^7F_2$ transition were found to be better than those registered for Eu^{3+} in lead boro-telluro-phosphate glasses [27]. However, it was close to those registered for Eu^{3+} doped lead fluoroborate glasses [43] which indicated their potential for laser applications. It was asserted that Eu^{3+} activated and MNPs embedded BT glass system was suitable for visible red laser applications as well as optical display devices at around 614 nm.

Table 5
J-O ($\times 10^{-20}cm^2$) intensity parameter of all prepared BT glass samples.

Glass code	J-O Parameters			Trends of Ω_λ	Ref.
	Ω_2	Ω_4	Ω_6		
BTMEMn0.0	3.44	0.85	Insignificant	$\Omega_2 > \Omega_4 > \Omega_6$	Present work
BTMEMn0.5	3.48	0.86	Insignificant	$\Omega_2 > \Omega_4 > \Omega_6$	Present work
BTMEMn1.0	3.50	0.91	Insignificant	$\Omega_2 > \Omega_4 > \Omega_6$	Present work
BTMEMn1.5	3.25	0.90	Insignificant	$\Omega_2 > \Omega_4 > \Omega_6$	Present work
BTMEMn2.0	2.67	0.72	Insignificant	$\Omega_2 > \Omega_4 > \Omega_6$	Present work
Eu:PbLFB	2.73	0.16	0	$\Omega_2 > \Omega_4 > \Omega_6$	[43]
SLBPEu	2.98	0.42	0	$\Omega_2 > \Omega_4 > \Omega_6$	[33]
GICZPSEu	1.36	0.25	0	$\Omega_2 > \Omega_4 > \Omega_6$	[27]
BPAEu	3.33	0.55	0	$\Omega_2 > \Omega_4 > \Omega_6$	[30]

3.6. Luminescence decay

Fig. 7 shows the decay curves of $^5D_0$ level for various concentrations of MNPs under 390 nm excitations ($^7F_0 \rightarrow {}^5D_2$) while the emission is monitored at 615 nm. The decay curves of all the prepared glasses were found to be single exponential and listed in Table 6. The excited state lifetime was evaluated using the below given expression,

$$I_t = I_0 e^{-t/\tau} \quad (12)$$

where I_t and I_o are the luminescence intensities at time $t = 0$ and at 't' respectively, τ is the lifetime of the excited level.

The estimated experimental lifetime (τ_{exp}) values were found to be 1.02, 0.86, 0.78, 0.72, and 0.48 ms corresponding to the BTMEMn0.0, BTMEMn0.5, BTMEMn1.0, BTMEMn1.5 and BTMEMn2.0 glasses, respectively. It was clear that addition of MNPs has significantly changed the lifetime even at very low concentration (0.5 mol %). These observations were supported by the findings of Wan et al. [44] on decay analysis of manganese ions in oxide glasses. It is well known that due to the presence of exchange interaction, the spin selection rule take place. Consequently, it reduced the lifetime of emission. This lifetime reduction at higher concentrations of MNPs caused the formation of exchange coupled Mn pairs. Additionally, at room temperature the lifetime was reduced by thermal quenching, which was found to be sample dependent. The values of τ_{exp} for BT glasses were comparable or slightly lower than those of other glass system such as tellurite (0.793 ms) [32], borophosphate (2.30 ms) [33] and phosphate (2.34–2.47 ms) [35] which were commonly studied for efficient red emission. Infact, others glasses caused significant changes in the values for the lifetime.

The increasing nature asymmetry around the Eu^{3+} ion sites was confirmed through the luminescence intensity ratio (LIR) which was responsible lifetime shortening [30]. Meanwhile, the radiative lifetime for the prepared BTMEMn0.0, BTMEMn0.5, BTMEMn1.0, BTMEMn1.5 and BTMEMn2.0 glasses obtained using the J-O theory was 2.08, 1.86, 1.52, 1.83 and 2.89 ms, respectively (Table 6). It was observed that τ_{exp} values were lower than τ_{cal} values. The discrepancy between τ_{exp} and τ_{cal} values was characterized through the non-radiative relaxation rate (W_{MPR}) of the excited Eu^{3+} ions. The multiphonon relaxation rate was calculated according to the expression:

$$W_{MPR} = \frac{1}{\tau_{exp}} - \frac{1}{\tau_{cal}} \quad (13)$$

Table 6
Emission band position (λ_p, nm), effective bandwidth ($\Delta\lambda_{eff}$, nm), radiative transition probability (A, s^{-1}), stimulated emission cross-section σ ($\times 10^{-22}$ cm^2), branching ratios (β_R), experimental (τ_{exp}) and calculated (τ_{cal}) lifetimes and quantum efficiency (η) of the Eu^{3+}: MNPs synthesis magnesium BT glasses.

Transition $^5D_0$ →	Parameters	BTMEMn0.0	BTMEMn0.5	BTMEMn1.0	BTMEMn1.5	BTMEMn2.0
$^7F_1$	λ_p	591	591	591	591	590
	$\Delta\lambda_{eff}$	11.88	11.69	12.03	12.00	11.73
	A	148.24	160.11	185.81	170.31	166.86
	σ	3.75	3.92	3.99	3.89	3.95
	β_R	21.57	21.00	20.02	21.57	29.21
$^7F_2$	λ_p	614	614	614	614	613
	$\Delta\lambda_{eff}$	11.19	11.12	11.40	11.44	11.69
	A	481.25	537.99	658.28	545.69	346.06
	σ	4.44	16.11	17.41	15.22	9.61
	β_R	70.00	70.50	70.97	69.01	60.78
$^7F_4$	λ_p	699	699	699	699	699
	$\Delta\lambda_{eff}$	12.38	12.40	13.02	12.99	11.48
	A	58.02	64.90	83.58	74.50	57.02
	σ	2.76	3.27	3.25	3.07	2.49
	β_R	8.44	8.50	9.01	9.42	10.01
τ_{cal} (ms)		2.89	2.08	1.52	1.83	2.89
τ_{exp} (ms)		0.73	1.02	0.89	0.78	0.64
η (%)		25	49	59	43	34

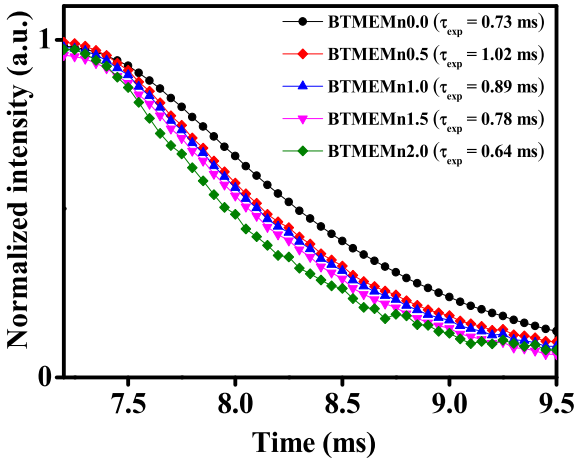

Fig. 7. Decay curves of the $^5D_0$ excited state of the synthesized BT glasses.

The calculated values of W_{MPR} for the BTMEMn0.0, BTMEMn0.5, BTMEMn1.0, BTMEMn1.5, and BTMEMn2.0 samples were 0.99, 0.44, 0.47, 0.74 and 1.02 s^{-1}, respectively. The multiphonon relaxation rate was effectively reduced which in turn enhanced the radiative emission. The quantum efficiency was defined as the rate of number of photons emitted to the number of photons absorbed. For RE ion doped glasses, it was determined as the ratio of the experimental lifetime to the calculated lifetime via:

$$\eta = \frac{\tau_{exp}}{\tau_{cal}} \times 100 \quad (14)$$

The estimated values of quantum efficiency corresponding to BTMEMn0.0, BTMEMn0.5, BTMEMn1.0, BTMEMn1.5, and BTMEMn2.0 glasses were 33%, 55%, 59%, 43% and 25%, respectively. The quantum efficiency was increased considerably with increasing concentration of MNPs included in the prepared glasses. The quantum efficiency of the present BTMEMn glasses was higher than those registered for Eu^{3+} doped magnesium borotellurite glass (39%) [45] and lead boro-tellurite-phosphate glass (46%) [43].

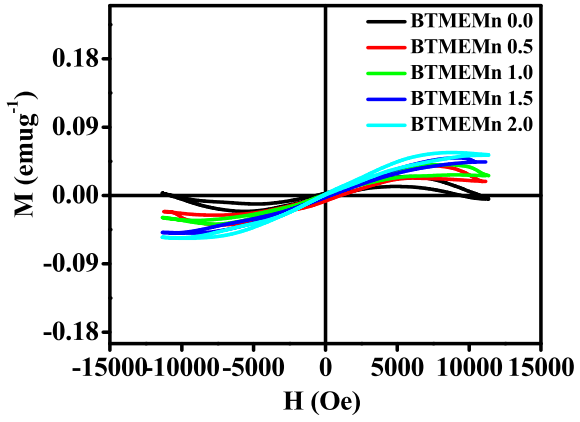

Fig. 8. M-H curve of the prepared borotellurite glasses.

3.7. Magnetic properties

3.7.1. Vibrating sample magnetometer measurement

Fig. 8 shows the room temperature magnetization versus external magnetic field (M-H) curves recorded of the glass system as a function of MNPs concentration change. The value of saturation magnetization (M_s), remanent magnetization (M_r), squareness (M_r/M_s), coercivity (H_c) and susceptibility (χ) of the prepared NPs are enlisted in Table 7.

The observed enhancement in the magnetization with the addition of MNPs was ascribed to the NPs magnetic moment alignment towards the applied field [46]. The magnetic interaction among the magnetic Mn ions in the glass matrix played a role in such augmentation of magnetic properties. This was ascribed to the difference in the surrounding of magnetic atoms which was contributed by the spin configuration in the core and surface area of magnetic particles as reported earlier [47]. Furthermore, the remanent magnetization was also increased with the addition of MNPs. This was due to the presence of single domain grain structure with a domain specific atomic field direction. This atomic direction remained unaffected by the influence of external magnetic field which contributed to the rotation domain and produced large energy thus enhanced the magnetization. As evident in Table 7, the squareness (M_r/M_s) of BTMEMn glasses varied with the increase of MNPs concentrations and the highest value was achieved for BTMEMn1.0 glass. The calculated value of H_c was ranged from 4.19 to 1424.42 Oe. It was slightly increased for MNPs contents up to 1.0 mol % and decreased beyond this value. The BTMEMn1.0 glass

Table 7
Magnetic properties of prepared BT glasses.

Sample	Magnetic parameters							
	M_s (emug^{-1}) $\times 10^{-2}$	M_r (emug^{-1}) $\times 10^{-3}$	H_c (Oe)	M_r/M_s (emug^{-1}) $\times 10^{-2}$	χ_m (emuOe^{-1}g^{-1}) $\times 10^{-6}$	g-values	H_r (Oe)	ΔH_{pp} (Oe)
BTMEMn0.0	4.95 ± 0.25	0.61 ± 0.03	128.25 ± 6.41	1.36 ± 0.06	4.12 ± 0.21	1.99 ± 0.01	201.52 ± 0.81	79.17 ± 1.58
BTMEMn0.5	5.45 ± 0.25	0.97 ± 0.01	162.01 ± 8.10	1.78 ± 0.08	4.54 ± 0.23	1.95 ± 0.01	218.82 ± 0.87	121.74 ± 2.43
BTMEMn1.0	8.11 ± 0.41	4.06 ± 0.2	1424.42 ± 71.22	5.01 ± 0.25	6.76 ± 0.34	1.89 ± 0.01	226.49 ± 0.91	136.47 ± 2.72
BTMEMn1.5	8.49 ± 0.43	2.30 ± 0.10	81.61 ± 4.08	2.71 ± 0.13	7.08 ± 0.35	1.90 ± 0.01	225.82 ± 0.90	129.87 ± 2.59
BTMEMn2.0	13.31 ± 0.65	2.13 ± 0.11	4.19 ± 0.20	1.61 ± 0.08	11.09 ± 0.55	1.98 ± 0.01	211.88 ± 0.84	84.82 ± 1.69

was observed to exhibit the highest H_c which was responsible for the enhancement of magnetizations (see Table 7). The increase of coercivity explained the increase of surface anisotropy in a spin-glass-like state [48]. The magnetic susceptibility of the glass system was calculated from Ref. [48]:

$$M = \chi_m H \tag{15}$$

where χ_m is the magnetic susceptibility, M is a magnetization and H is a field. The susceptibility of prepared glasses was increased with the increase of MNPs concentrations. The single Eu^{3+} ion anisotropy has affected the MNPs local field environment where the main contribution was from the changes of electron spin. Hence, the presence of MNPs in BTMEMn glass with positive susceptibility confirmed that the material revealed paramagnetic behaviour.

3.7.2. Electron spin resonance spectra

ESR spectra of Eu^{3+} doped magnesium BT glasses embedded with various concentrations of MNPs was recorded and presented in Fig. 9. ESR was used to detect paramagnetic behaviour and to provide information about the coordination of isolated sites. The calculated values of magnetic parameters such as resonance magnetic field (H_r), peak-to-peak line width (ΔH_{pp}) and g-factor are obtained by ESR spectra were summarized in Table 7. The magnetic resonance spectra are dominated by the intense and broad line. The broadening of the EPR spectra usually observed in anisotropic antiferromagnets due to the slowing down of spin fluctuations. It was caused by the presence of defects in the nanopowder leading to strains thus produced a broad distribution of the magnetic anisotropy interactions [25]. The shift of the centre of resonance to the lower fields at higher concentration may be due to nonhomogeneous local magnetic field that modified the resonance field. The introductions of MNPs in glass matrix were responsible in ligand-field effect which was caused by the variation in the interaction of outer electron (3d shell) with the inner electron (4*f* shell). Consequently, the local environment of manganese was changed that contributed to the non-symmetrical curve (Fig. 9).

ESR spectra detected the presence of Mn^{2+} and Mn^{4+} ions in the glass, whereas Mn^{3+} was not detected due to the complete splitting of the energy levels [49]. When MNPs were introduced in BTMEMn glass, the ESR spectra showed resonance lines as Mn^{2+} ions were entered in the glass as paramagnetic probes. This can be considered as a superposition of two overlapping signals for all concentrations of MNPs. The highest signal intensity of manganese was displayed for concentration of 2.0 mol %. The contribution of this signal was due to the increase of manganese ions and the absence of antiferromagnetic interaction between manganese ions in the glass system. The increment in the intensity of the signal depended on the concentration of magnetic ions. The induced magnetic field (exchange anisotropy field) was the main source of magnetic moments for these glass systems [50]. Furthermore, the number of unpaired electrons was different in different oxidation states. This could be easily distinguished from the number of fine transitions in the ESR

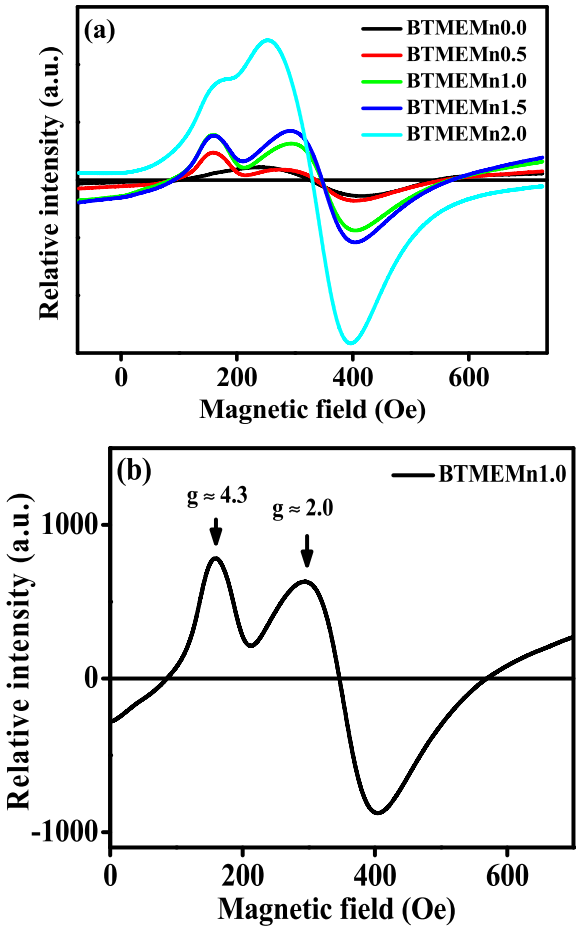

Fig. 9. (a) ESR spectra of Eu^{3+}: Mn doped BT glasses (b) ESR spectra of MNPs at 1.0 mol %.

spectra from their *g* value [51]. The *g* value was also indicative of the nature of the bonding. The bonding is said to be ionic if the *g* value shows a negative shift with respect to the free electron *g* value (2.0023). Conversely, if the shift is positive, the bonding is said to be more covalent in nature.

In the present work, the rather positive shift in the *g* value (1.99–1.89 = +0.10) was observed as concentration MNPs in the glass was increased. The value of g = 1.89 is the minimum one where the bond is in covalence environment as shown by BTMEMn1.0 sample. All the glass samples with MNPs embedment exhibited two resonance signals at $g \approx 1.9$ and $g \approx 4.3$ which were characteristic of manganese ion. The position of $g \approx 1.9$ occurred due to Mn ions coupled by the exchange that could effect of the site Mn^{2+} ion, which was expected to replace the TeO^{2+} ion in an environment that is close to octahedral symmetry. Meanwhile, the resonance at $g \approx 4.3$ was attributed to the rhombic surroundings of

the Mn^{2+} ions [52]. It was observed that the intensity of the signal *g* at 1.9 was more intense compared to *g* values at 4.3. This indicated that more number of Mn^{2+} centers was present in an octahedral environment than in the rhombic environment [53]. Table 7 revealed that the calculated values of ΔH_{pp} was increased from 79.17 ± 1.58 to 139.47 ± 2.73 Oe and the values of *g* were decreased from 1.99 to 1.89 when the concentration of MNPs was increased. This variations of ΔH_{pp} and *g* value were due to stronger dipole–dipole interactions and super-exchange interactions [54]. Table 7 also showed that the value of the resonant magnetic field was increased from 201.52 ± 0.81 to 226.49 ± 0.91Oe as the concentration of MNPs was increased up to 1.0 mol % and decreased thereafter. Values of g were calculated using:

$$g = h\nu/\beta H \quad (16)$$

where *h* is Planck's constant, ν is the microwave frequency, β is the Bohr magneton (9.274×10^{-21} erg Oe^{-1}), and H is resonant magnetic field, the resonance magnetic field should decrease when the *g* increases, whereas ν is constant in EPR spectroscopy. Addition of Mn^{2+} ions in to the glass matrices caused an increase in the super-exchange interactions, contributing to the increase of the internal field and decrease of the resonance magnetic field. These results provided the clear evidence of surface contribution to the observed magnetic properties. This was supported by the magnetic properties via M-H curves. The magnetic field dependence of magnetization M-H curves exhibits hysteresis behaviour at optimum concentration 1.0 mol % with higher M_r and H_c values was due to the large surface anisotropy present on the glass matrices. EPR spectra strongly indicated that Mn^{2+} centers were in asymmetric sites (octahedral) and the nature of the bonding was dominantly covalent type.

4. Conclusion

The effects of MNPs inclusion on the structural, optical and magnetic properties of Eu^{3+} doped BT glass system were determined. Such glass system was prepared using melt quenching method and thoroughly characterized. XRD pattern confirmed the amorphous natures of prepared glasses and HR-TEM image verified the existence of NPs inside the glass matrix. Furthermore, SAED pattern revealed the d-spacing of MNPs ≈0.276 nm with the growth orientation along (103) lattice planes. The value of nephelauxetic ratio displayed covalent nature of prepared glasses. The observed luminescence quenching was attributed to the energy transfer from europium ion to NPs. The value of Ω_2 exhibited the strong dependence of covalency between RE ion and ligand ions. Among the studied glasses, BTMEMn1.0 glass displayed the highest value of A, β_R and σ corresponding to the $^5D_0 \rightarrow {}^7F_2$ transition as well as maximum quantum efficiency. Glass system incorporated with MNPs showed paramagnetic hysteresis. It was concluded that the BTMEMn1.0 glass having interesting optical and magnetic properties were beneficial for wide range of applications including magneto-optic devices and visible lasers operating at emission wavelength of 614 nm.

Acknowledgments

The authors gratefully acknowledge the financial support from UTM and Malaysian Ministry of Education through the Vot. 4L657, 4F752 and 12H42, 05H45, 17H19 and 13H50 (GUP).

References

[1] R.J. Amjad, M.R. Dousti, M.R. Sahar, S.F. Shaukat, S.K. Ghoshal, E.S. Sazali, Silver nanoparticles enhanced luminescence of Eu^{3+}-doped tellurite glass, J. Lumin. 154 (2014) 316–321.
[2] Z.A.S. Mahraz, M. Sahar, S. Ghoshal, M. Dousti, R. Amjad, Silver nanoparticles enhanced luminescence of Er^{3+} ions in boro-tellurite glasses, Mat. Lett. 112 (2013) 136–138.
[3] N.M. Yusoff, M.R. Sahar, Effect of silver nanoparticles incorporated with samarium-doped magnesium tellurite glasses, Phys. B: Condens. Matter 456 (2015) 191–196.
[4] H. Fares, W. Stambouli, H. Elhouichet, B. Gelloz, M. Férid, Nano-silver enhanced luminescence of Er^{3+} ions embedded in tellurite glass, vitro-ceramic and ceramic: impact of heat treatment, RSC Adv. 6 (2016) 31136–31145.
[5] M. Alagiri, C. Muthamizhchelvan, S. Ponnusamy, Structural and magnetic properties of iron, cobalt and nickel nanoparticles, Synth. Met. 161 (2011) 1776–1780.
[6] V.C. Bose, V. Biju, Optical, electrical and magnetic properties of nanostructured Mn3O4 synthesized through a facile chemical route, Phys. E Low-Dimens. Syst. Nanostruct. 66 (2015) 24–32.
[7] H. Dhaouadi, O. Ghodbane, F. Hosni, F. Touati, Mn_3O_4 nanoparticles: synthesis, characterization and dielectric properties, ISRN Spectrosc. (2012) 1–8.
[8] H. Dhaouadi, A. Madani, F. Touati, Synthesis and spectroscopic investigations of Mn_3O_4 nanoparticles, Mater. Lett. 64 (2010) 2395–2398.
[9] J. Pike, J. Hanson, L. Zhang, S. Chan, Synthesis and redox behavior of nanocrystalline Hausmannite (Mn_3O_4), Chem. Mater. 42 (2007) 5609–5616.
[10] S. Yusub, P. Srinivasa Rao, D. Krishna Rao, Ionic conductivity, dielectric and optical properties of lithium lead borophosphate glasses combined with manganese ions, J. Alloys Compd. 663 (2016) 708–717.
[11] S.P. Hashim, H.A. Sidek, M.K. Halimah, K.A. Matori, W.M. Yusof, M.H. Zaid, The effect of remelting on the physical properties of borotellurite glass doped with manganese, Int. J. Mol. Sci. 14 (2013) 1022–1030.
[12] B. Sumalatha, I. Omkaram, T. Rajavardhana Rao, C. Linga Raju, The structural, optical and magnetic parameter of manganese doped strontium zinc borate glasses, Phys. B Condens. Matter 411 (2013) 99–105.
[13] B. Peng, T. Izumitani, The fluorescence properties of Eu^{3+} in various glasses and the energy transfer between Eu^{3+} and Sm^{3+} in borosilico-phosphate glass, Rev. Laser Eng. 22 (1994), 16–16.
[14] R. Van Deun, K. Binnemans, C. Görller-Walrand, J.L. Adam, Judd-Ofelt intensity parameters of trivalent lanthanide ions in a $NaPO_3$-BaF_2 based fluorophosphate glass, J. Alloys Compd. 283 (1999) 59–65.
[15] B.R. Judd, Optical absorption intensities of rare-earth ions, Phys. Rev. 127 (1962) 750–761.
[16] K. Maheshvaran, P.K. Veeran, K. Marimuthu, Structural and optical studies on Eu^{3+} doped boro-tellurite glasses, Solid State Sci. 17 (2013) 54–62.
[17] K. Selvaraju, K. Marimuthu, T. Seshagiri, S. Godbole, Thermal, structural and spectroscopic investigations on Eu^{3+} doped boro-tellurite glasses, Mater. Chem. Phys. 131 (2011) 204–210.
[18] A. Vazquez-Olmos, R. Redon, G. Rodriguez-Gattorno, M. Esther Mata-Zamora, F. Morales-Leal, A.L. Fernandez-Osorio, One-step synthesis of Mn_3O_4 nanoparticles: structural and magnetic study, J. Colloid Interface Sci. 291 (2005) 175–180.
[19] S. Zheng, Y. Zhou, D. Yin, X. Xu, X. Wang, Influence of WO_3 on the spectroscopic properties and thermal stability of Er^{3+}/Ce^{3+} codoped tellurite glasses, Opt. Mater. 35 (2013) 1526–1531.
[20] R. Kundu, S. Dhankhar, R. Punia, K. Nanda, N. Kishore, Bismuth modified physical, structural and optical properties of mid-IR transparent zinc borotellurite glasses, J. Alloys Compd. 587 (2014) 66–73.
[21] N. Kaur, A. Khanna, Structural characterization of borotellurite and alumino-borotellurite glasses, J. Non-Cryst. Solids 404 (2014) 116–123.
[22] M.H. Bhat, K. Rao, Investigation of the mixed alkali effect in boro-tellurite glasses-the role of NBO-BO, Curr. Sci. 86 (2004).
[23] M.A. Pandarinath, G. Upender, K.N. Rao, D.S. Babu, Thermal, optical and spectroscopic studies of boro-tellurite glass system containing ZnO, J. Non-Cryst. Solids 433 (2016) 60–67.
[24] C. Pfeiffer, C. Rehbock, D. Huhn, C. Carrillo-Carrion, D.J. de Aberasturi, V. Merk, Interaction of colloidal nanoparticles with their local environment: the (ionic) nanoenvironment around nanoparticles is different from bulk and determines the physico-chemical properties of the nanoparticles, J. R. Soc. Interface 11 (2014) 20130931.
[25] I. Djerdj, D. Arčon, Z. Jagličic, M. Niederberger, Nonaqueous synthesis of manganese oxide nanoparticles, structural characterization, and magnetic properties, J. Phys. Chem. C 111 (2007) 3614–3623.
[26] E.G. Nicholas, E.S. Charles, Luminescence Spectroscopy, first ed., Academic Press INC, New Work, 2000.
[27] S. Selvi, K. Marimuthu, N. Suriya Murthy, G. Muralidharan, Red light generation through the lead boro-telluro-phosphate glasses activated by Eu^{3+} ions, J. Mol. Struct. 1119 (2016) 276–285.
[28] M.V. Vijaya Kumar, B.C. Jamalaiah, K. Rama Gopal, R.R. Reddy, Novel Eu^{3+}-doped lead telluroborate glasses for red laser source applications, J. Solid State Chem. 184 (2011) 2145–2149.
[29] M. Dejneka, E. Snitzer, R. Riman, Blue, green and red fluorescence and energy transfer of Eu^{3+} in fluoride glasses, J. Lumin. 65 (1995) 227–245.
[30] R. Vijayakumar, K. Marimuthu, Luminescence studies on Ag nanoparticles embedded Eu^{3+}doped boro-phosphate glasses, J. Alloys Compd. 665 (2016) 294–303.
[31] V.P. Tuyen, T. Hayakawa, M. Nogami, J.R. Duclère, P. Thomas, Fluorescence line

narrowing spectroscopy of Eu^{3+} in zinc–thallium–tellurite glass, J. Solid State Chem. 183 (2010) 2714–2719.
[32] A.M. Babu, B.C. Jamalaiah, T. Suhasini, T.S. Rao, L.R. Moorthy, Optical properties of Eu^{3+}ions in lead tungstate tellurite glasses, Solid State Sci. 13 (2011) 574–578.
[33] N. Kiran, Eu^{3+} ion doped sodium-lead borophosphate glasses for red light emission, J. Mol. Struct. 1065–1066 (2014) 93–98.
[34] C. Zhu, S. Chaussedent, S. Liu, Y. Zhang, A. Monteil, N. Gaumer, Composition dependence of luminescence of Eu and Eu/Tb doped silicate glasses for LED applications, J. Alloys Compd. 555 (2013) 232–236.
[35] G.H. Silva, V. Anjos, M.J.V. Bell, A.P. Carmo, A.S. Pinheiro, N.O. Dantas, Eu^{3+} emission in phosphate glasses with high UV transparency, J. Lumin. 154 (2014) 294–297.
[36] G.S. Ofelt, Intensities of crystal spectra of rare-earth ions, J. Chem. Phys. 37 (1962) 511.
[37] M.R. Dousti, G.Y. Poirier, A.S.S. de Camargo, Structural and spectroscopic characteristics of Eu^{3+}-doped tungsten phosphate glasses, Opt. Mater. 45 (2015) 185–190.
[38] P. Manasa, C.K. Jayasankar, Luminescence and phonon side band analysis of Eu^{3+}-doped lead fluorosilicate glass, Opt. Mater. 62 (2016) 139–145.
[39] M. Ferhi, C. Bouzidi, K. Horchani-Naifer, H. Elhouichet, M. Ferid, Judd–Ofelt analysis of spectroscopic properties of Eu_{3+} doped $KLa(PO_3)_4$, J. Lumin. 157 (2015) 21–27.
[40] A. Awang, S.K. Ghoshal, M.R. Sahar, M. Reza Dousti, R.J. Amjad, F. Nawaz, Enhanced spectroscopic properties and Judd-Ofelt parameters of Er-doped tellurite glass: effect of gold nanoparticles, Curr. Appl. Phys. 13 (2013) 1813–1818.
[41] R. Reisfeld, E. Greenberg, R. Brown, M. Drexhage, C. Jørgensen, Fluorescence of europium (III) in a flouride glass containing zirconium, Chem. Phys. Lett. 95 (1983) 91–94.
[42] J. Amjad, M.R. Dousti, M.R. Sahar, Spectroscopic investigation and Judd–Ofelt analysis of silver nanoparticles embedded Er^{3+}-doped tellurite glass, Curr. Appl. Phys. 15 (2015) 1–7.
[43] S. Arunkumar, K. Venkata Krishnaiah, K. Marimuthu, Structural and luminescence behavior of lead fluoroborate glasses containing Eu^{3+} ions, Phys. B Condens. Matter 416 (2013) 88–100.
[44] M.H. Wan, P.S. Wong, R. Hussin, H.O. Lintang, S. Endud, Structural and luminescence properties of Mn^{2+} ions doped calcium zinc borophosphate glasses, J. Alloys Compd. 595 (2014) 39–45.
[45] K. Maheshvaran, K. Marimuthu, Concentration dependent Eu^{3+} doped borotellurite glasses-Structural and optical investigations, J. Lumin. 132 (2012) 2259–2267.
[46] L. Zhang, Y. Zhang, Fabrication and magnetic properties of Fe_3O_4 nanowire arrays in different diameters, J. Magn. Magn. Mater. 321 (2009) L15–L20.
[47] P. Hu, S. Zhang, H. Wang, D. Pan, J. Tian, Z. Tang, Heat treatment effects on Fe_3O_4 nanoparticles structure and magnetic properties prepared by carbothermal reduction, J. Alloy Compd. 509 (2011) 2316–2319.
[48] M. Tadić, M. Panjan, D. Marković, I. Milošević, V. Spasojević, Unusual magnetic properties of NiO nanoparticles embedded in a silica matrix, J. Alloy Compd. 509 (2011) 7134–7138.
[49] V. Singh, R.P.S. Chakradhar, J.L. Rao, D.-K. Kim, EPR and luminescence properties of combustion synthesized $LiAl_5O_8$:Mn phosphors, Mat. Chem. Phys. 110 (2008) 43–51.
[50] S. Sambasivam, G.J. Li, J.H. Jeong, B.C. Choi, Structural, optical, and magnetic properties of single-crystalline Mn_3O_4 nanowires, J. Nanopart Res. 14 (2012) 1138.
[51] N. Srisittipokakun, C. Kedkaew, J. Kaewkhao, Electron spin resonance (ESR) and optical absorption spectra of a manganese doped soda-lime-silicate glass system, Kasetsart J. (Nat. Sci.) 43 (2009) 360–364.
[52] R.P. Sreekanth Chakradhar, G. Sivaramaiah, J.L. Rao, N.O. Gopal, EPR and optical investigations of manganese ions in alkali lead tetraborate glasses, Spectrochim. Acta - Part A Mol. Biomol. Spectrosc. 62 (2005) 761–768.
[53] M. Augustin, D. Fenske, L. Bardenhagen, A. Westphal, Manganese oxide phases and morphologies: a study on calcination temperature and atmospheric dependence, Beilstein J. Nanotechnol. 6 (2015) 47–59.
[54] M.G. Naseri, E.B. Saion, M. Hashim, A.H. Shaari, A.H. Ahangar, Synthesis and characterization of zinc ferrite nanoparticles by a thermal treatment method, Solid State Commun. 151 (2011) 1031–1035.